Applied Surface Science 496 (2019) 143594

Contents lists available at ScienceDirect

Applied Surface Science

journal homepage: www.elsevier.com/locate/apsusc

Full length article

Effects of radiative local heating on metal solidification during selective laser melting for additive manufacturing

Beom Seok Kim[a,1], Namkyu Lee[b,1], Subhash Thota[c], Thomas Gemming[d], Hyung Hee Cho[b,*]

[a] Nuclear Fusion Research Institute, 169-148 Gwahak-ro, Yuseong-gu, 34133 Daejeon, Republic of Korea
[b] Department of Mechanical Engineering, Yonsei University, Yonsei-ro 50, 03722 Seoul, Republic of Korea
[c] Department of Physics, Indian Institute of Technology Guwahati, 781 039, Assam, India
[d] IFW Dresden, P. O. Box 270116, 01171 Dresden, Germany

ARTICLE INFO

Keywords:
Selective laser melting
Radiative heat absorption
Conductive heat dissipation
Thermal design
Additive manufacturing
Marangoni flow

ABSTRACT

Selective laser melting (SLM) is a promising additive manufacturing technique arising from glassy metal characteristics of treated medium. When creating novel compositions of materials and intricate workpieces, reliable thermal designs should be implemented based on well-understood heat transfer characteristics on matierlas to be used. Herein, we investigate local and overall heat transfer characteristics of SLM processes and investigate the principal parameters related to the magnituge of a radiative heating power and its exposure time. We present how to exert their influence upon local melting and sequential solidification of copper powder bed. The local solid media reach a quasi-equilibrium state in even 1 ms with the incident powers of 50, 100, and 200 W. The anisotropic expansion of the molten pool is governed by a thermally-induced Marangoni flow. As the power is increased, the Marangoni factor increases linearly up to 853.7%. Consequential heat transfer characteristics tell us that unconditional input power should be avoided to prohibit the detrimental effect; the radiative heating power should be confined for thermalization of a target domain and for that preventing the evaporation of a material. These approaches from material science to heat transfer can be used to develop a platform for SLM processes guaranteeing its feasibility and applicability.

1. Introduction

Since mankind has used tools, designing and fabricating mechanical components have been key technologies for upgrading industries, involving development novel systems and improvements of conventional energy transferring systems, as well as for the survival of mankind itself. In modern engineering systems such as gas turbines and power propulsion devices, complex geometric components have been used. These components enable us to obtain high performance, efficiency, improved cooling and energy transfer against their mechanical failure. Critical and technical demands, such as more complicated geometries for improving reliability of those components, are growing. However, it is difficult to make intricate components using conventional fabrication techniques. As of now, that is why a three-dimensional (3D) printing technologies are considered promising tools for driving future industrialization, so called industry 4.0 [1,2].

Additive manufacturing, as opposed to subtractive methodologies, can be used to develop novel methodologies for synthesizing and fabricating complicated structures from even metallic materials [3–6]. Radiative energy sources are used for local deformation (*i.e.*, thermalization) of the target materials during sintering and melting. Selective laser melting (SLM) can be used to fabricate parts with complex geometries directly from powder feedstocks [7,8]. Fig. 1 shows a schematic of the SLM process with a target powder material. SLM is advantageous for manufacturing sophisticated and large-scale parts. Because components are fabricated layer by layer in a bottom-up process, SLM can be used to fabricate free-standing pieces and does not rely on specific molds [9]. A very dense workpiece can be obtained by completely melting the metallic particles then immediately solidifying them, and no post-processing steps are required. Local heating and cooling can potentially be used to make glassy metal as the high cooling rate required for vitrification is obtainable during the SLM process. Metallic glasses can have complex geometries and desirable properties such as mechanical strength, corrosion resistance, and high magnetic applicability [9–12]. Regarding to its process based on powder metallurgy, there is a wide variety of materials which can be used for making

* Corresponding author.
E-mail address: hhcho@yonsei.ac.kr (H.H. Cho).
[1] Equally contributed.

https://doi.org/10.1016/j.apsusc.2019.143594
Received 19 March 2019; Received in revised form 14 July 2019; Accepted 4 August 2019
Available online 05 August 2019
0169-4332/

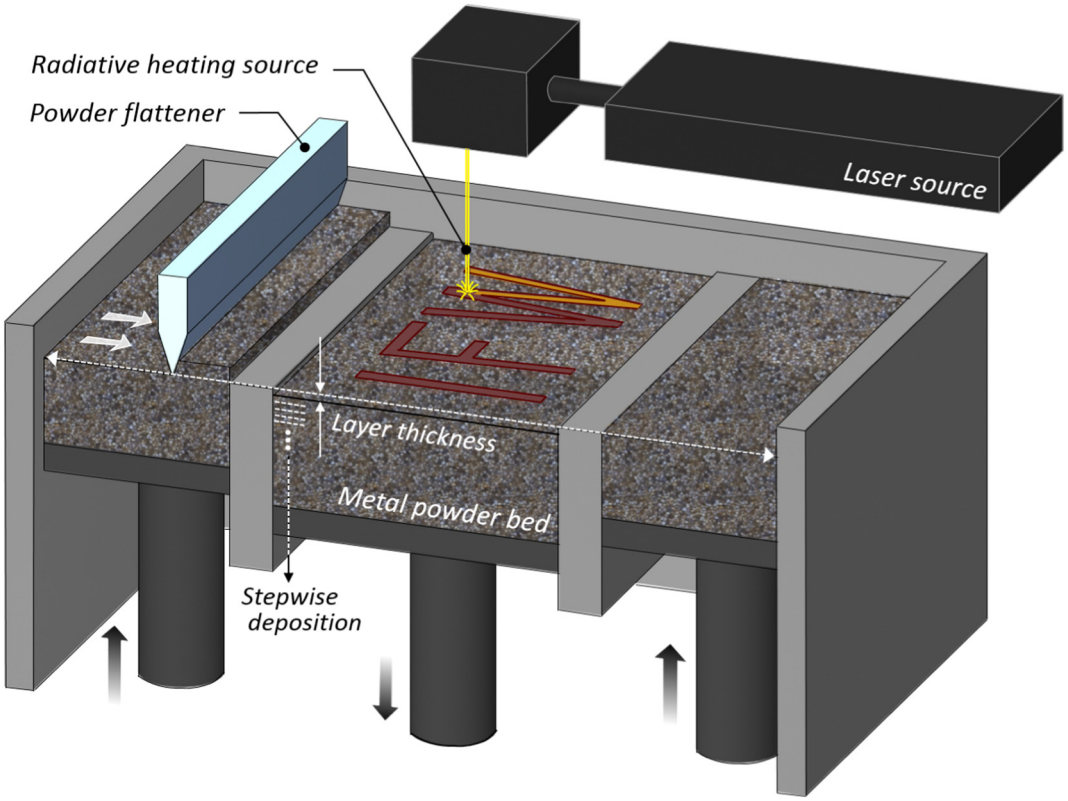

Fig. 1. Schematic diagram of selective laser melting (SLM). Based on computer-aided design, planar patterns are drawn using a high-power laser to induce local thermalization. The planar structure is deposited in layers and a 3 dimensional workpiece is manufactured by repeating the planar drawing whilst vertically moving the workpiece-lathe and feeding in the powder.

workpieces and whole components using SLM. Such components include gas turbine systems, turbine vane of airplanes, and multi-functional 3-D meta-structures [8,13–16].

What are principal parameters in additive manufacturing regarding thermal treatment in a series of thermal energy transfer? This has been still in questioning and should be resolved for further progresses to the extent of its feasibility and applicability. However, there exist complicated physical behaviors defining the process, such as the radiative heat transfer from the laser and subsequent heat-dissipating phenomena. SLM melting leads to thermal conditions where the transient temperature fluctuates from melting point to room temperature and there is a significant spatial gradient confined within a sub-millimeter area [17,18]. The variety of parameters that affect SLM makes full-scale experimental approaches difficult [18–21]. Thus, we have conducted a range of parameter studies, but are still in the early stages of understanding the effects of each parameter. Each novel material composition has a completely different parameter set. Regarding acceptable expenses of trial and error, analytical and numerical approaches, which partially reveal the fundamental physics based on thermodynamics and heat/energy transfer, can be used to optimize the parameters through '*thermal design*' [22–26].

In this study, we present a numerical approach for revealing the fundamental influence of different parameters on the subordinate domain. We used copper (Cu) powder as a base material due to its attractive merits of products such as high thermal and electrical conductivity for various applications [27–33]. Additionally, because of the high diffusive behavior of copper powder [34] by comparing other widespread materials such as Ni-alloys, Ti-alloys, Steels and Al-alloys which yields the difficult control, we thought that the copper powder is the most valuable material by adopting the thermal design process. Our methods take into account the difficulties described above. Under local heating conditions characterized by molten pool formation, we show that the power of the laser, in terms of input heat flux (*i.e.*, power per unit area), and the exposure time are the two principal factors determining a favorable local cooling rate for additive manufacturing. When vitrification is required, an appropriate cooling rated is required. Using qualitative and quantitative evaluations, we demonstrate local heat transfer characteristics with transient heat transfer responses leading to expansion of the molten pool size. The subsequent cooling rates vary in proportion to the applied power. To ensure appropriate melting and cooling rate performance, there should be an upper power limit corresponding to optimal conditions for diminishing the thermal Marangoni phenomenon. This phenomenon causes the homogeneity and designated pattern shape to deteriorate during solidification. Suitable parameters can be obtained using heat transfer analysis. The demonstrations on these parameters can then be used to guide the development of a framework for SLM techniques.

2. Materials and methods

2.1. Thermal design process for object function

The thermal design procedure is shown in Fig. 2. The procedure has the following steps: select the design variables and the domains of the design parameters; define boundary conditions based on the thermal properties of the material; analyze the transient local/overall heat transfer characteristics in terms of temperature variations; investigate the thermally induced variations in the characteristic molten pool size, the cooling rate and the Marangoni forces. The impact of the object functions, the optimal power and exposure time of radiative heating source, can be determined within a confined design domain. We focus on the thermal conditions required for melting a target area and the critical limit to prevent deterioration in performance. The performance deteriorates when the molten area expands beyond the intended

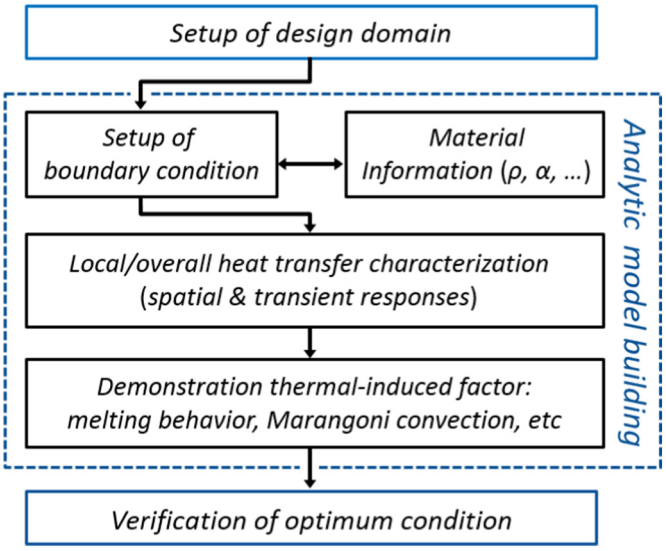

Fig. 2. Flow chart of the thermal design for characterizing heat transfer in SLM [26].

linewidth due to over-melting. This is primarily caused by the excess heat dissipation and Marangoni effects, which accompany the anisotropic expansion of the molten pool. Further details will be provided in the Results and Discussion section.

2.2. Modeling and design variables for characterizing heat transfer

2.2.1. Geometric domain set-up with material information

Fig. 3 shows the geometric domain used in our numerical analysis to investigate the heat transfer characteristics of the laser melting process. Our target structure is a standalone workpiece. We investigate the variations in transient heat transfer conditions as the system is exposed to the laser. We focus on the effects of the power and exposure time on stationary heating and subsequent cooling behaviors. These should be evaluated independently in advance so that we can then investigate parameters relating to the movements of the laser, such as velocity, hatch style, and layer thickness. Taking into account this object on the static but transient heat transfer conditions, we define our simulation domain to be a quarter of the full domain with symmetric conditions. The width (w) of the powder bed is 20 mm and the heights of the target material and substrate are both 10 mm. To reduce the complexity of the numerical analysis, the powder bed is treated as a homogeneously absorbing and scattering continuum; the effective thermal properties of the powder bed during radiative heat absorption and subsequent conductive and convective heat dissipation are equivalent to those of a solid model [8,24,35,36].

The thermo-physical properties of materials are classified as field or non-field properties [34]. Thermal conductivity, which is dependent on porosity, is a field property. However, the enthalpy and density, which are controlled by the mass of a given composition, are non-field properties. The field properties depend, in a complicated manner, on porosity and pore geometries. They are represented by a simplified generic relationship as $A_p = (1 - \varphi)A$, where A_p, A, and φ are the properties of the powder form, the bulk solid from, and the representative porosity, respectively [37–39]. The thermal conductivity of the powder depends on the geometric structure of the powder and is a function of the relative density, as follows [40]:

$$k_{eff} = k_{bulk}\frac{\phi}{1 + n(1 - \phi)^m} \quad (1)$$

where k_{eff} is the thermal conductivity of the target powder bed and ϕ is the relative density of copper powder, defined as $\rho_{powder}/\rho_{bulk}$, which is equal to 0.38 [25]. The relative density takes the porosity of the particles into account. n and m are experimentally determined constants with values of 11.73 and 0.78, respectively. The thermal conductivity of copper powder is 16.15 W/m·K. When the temperature of the target material is higher than the melting point of bulk copper (T_m = 1083 °C), we assume that the density and the thermal conductivity of the molten domain in the liquid phase are 8960 kg/m^3 and 386 W/m·K, respectively. The values for solid copper are the same. The density of bulk copper, ρ, is 8960 kg/m^3. Specific heat of bulk copper (380 J/kg·K) used in this calculation does not take into account the temperature-dependent relative density because the specific heat is principally a function of the mass fraction of a powder [41]. The Cu powder bed is placed on a stainless-steel substrate. The density, specific heat and thermal conductivity of the stainless-steel substrate are 7800 kg/m^3, 480 J/kg·K and 47 W/m·K, respectively [8].

2.2.2. Governing equations and boundary conditions

To analyze the thermal behavior on a target domain, we consider the energy equation as follows [42,43]:

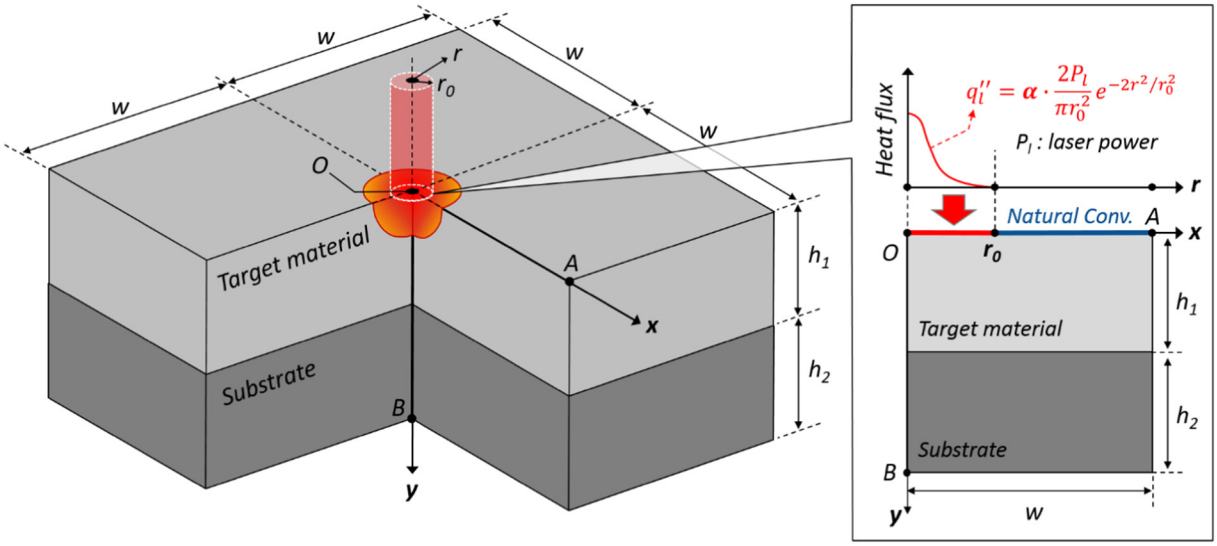

Fig. 3. Three-dimensional geometry used in numerical analysis, boundary conditions of a radiative heating source, and consequent heat transfer through the target powder bed.

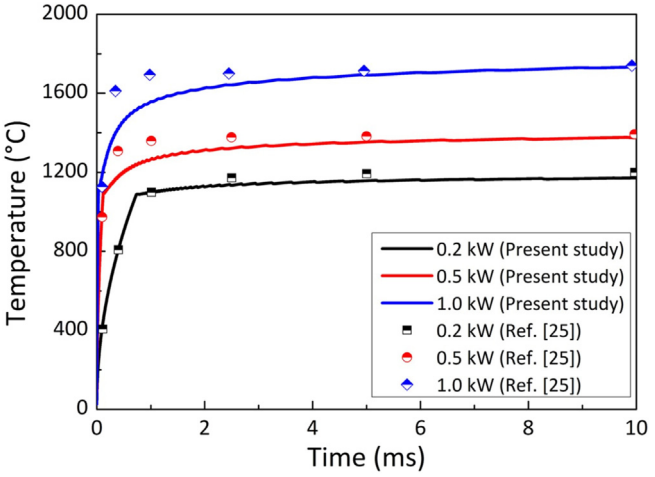

Fig. 4. Validation of numerical simulation data with reference which presents the numerical simulation with experimental data [25].

$$\rho c_p \frac{\partial T}{\partial t} = \nabla \cdot (k_{eff} \nabla T) + S_h \tag{2}$$

where ρ, c_p, T, t, and S_h are the density of the target medium, specific heat, temperature, time, and volumetric heat source, respectively. The commercial software package Fluent v.15.0 is used to analyze the effect of the laser heat source on the thermal behavior of the system. The characterization of the transient heat transfer is performed to evaluate the thermal response to the laser. The outward heat dissipation is modeled as convective heat transfer from the surface due to a purge gas of argon using Newton's cooling law as follows [43]:

$$q''_{conv} = h(T_f - T_w) \tag{3}$$

where h, T_f and T_w are the convective heat transfer coefficient, bulk fluid temperature and wall temperature, respectively. We assume that the heat transfer coefficient on the target material is 40 W/m^2·K, reflecting moderate natural convection due to a purge gas [25]. The heat transfer from the other surfaces around the domain is modeled as a conservative natural convection, with a coefficient of 5 W/m^2·K. The temperature of the fluids around the surfaces and initial temperature of the whole domain of the system is taken to be room temperature, which is 300 K. Radiative heat transfer occurs on the surfaces due to the temperature difference between the surfaces. When the system is in thermal equilibrium, the absorbance and the emissivity are the same [44]. In each step of the calculations, the results converge towards thermal equilibrium. We assume that the emissivity of the target powder bed is 0.4, which is the same as the absorbance of a target material [25,30]. We conducted a preemptive time-step test to evaluate the convergence and choose time step durations of 0.002 ms in this simulation. The total simulation time is 2 ms, with 1 ms each of heating and subsequent cooling. All simulations use double precision accuracy. The convergence criterion of the energy equation is 10^{-14}, which is sufficient for the system to converge at each time step.

We model the laser as a radiating heat source under surface heating conditions without any volumetric heating source. This model is plausible in the case of metallic powder beds as they have relatively short irradiance absorbance lengths in comparison to ceramic materials [23]; that is, S_h in Eq. (2) is null. The laser beam has an effective Gaussian beam power distribution with a symmetrical irradiance distribution. We assume that the laser irradiance is symmetric about the direction of propagation and, in most cases, the maximum irradiance of the power per unit area I_0 is at the center of the beam pattern. The beam irradiance of the fundamental mode is defined as $I(r) = I_0 e^{-2r^2/r_0^2}$, where r and r_0 are the radial distance from the center and the beam radius corresponding to the point where the irradiance diminishes to $1/e^2$, respectively [38]. Herein, r_0 is 35 μm. The inset in Fig. 3 describes the irradiance profile on the heating surface. Taking into account this radial distribution of the irradiance, we can use the expression for the input power of the laser to define the surface heat flux, q_l'', as follows [38]:

$$q_l'' = \frac{2P_l}{\pi r_0^2} e^{-2r^2/r_0^2} \tag{4}$$

where P_l is the laser power. We use a conventional ytterbium (Yb) laser with a wavelength of 1070 nm and powers of 50, 100 and 200 W, which are typical for laser-induced manufacturing [9]. They are equivalent to apparent surface heat flux of 1.3×10^6, 2.6×10^6, and 5.2×10^6 W/cm^2, respectively. The absorbance of a material α, where α is between zero and unity, depends on a number of factors including material composition, surface morphology, level of oxidation, wavelength of the irradiant source, and temperature [22,45]. We can quantify the correct input heat flux $\alpha \cdot q_l''$ in terms of the radiative absorbance, which is a quasi-interfacial property. The absorbance of the powder layer depends not only on its physicochemical properties but also on granulomorphology and apparent density. The absorbance of powder is substantially higher than that of the bulk materials [46]. The absorbance of a Cu powder bed with an average characteristic length of 45 μm in dense packing conditions is 0.4 [25,44].

For the numerical simulations, hexahedral structured meshes are used and their number is approximately 9.8 million. The grid is densely concentrated on the hot spot inside the irradiating laser radius (35 μm) and has edges of length 2 μm. This value is determined by preemptive grid independency tests. To access the numerical reliability, the results is compared to previously reported results and found to be in reasonable agreement with the average discrepancy less than 3.57% as shown in Fig. 4 [8,25].

3. Results and discussion

3.1. Heat transfer characteristics

3.1.1. Local heat transfer characteristics and temperature criteria (spatial and transient thermal responses)

Fig. 5 shows the spatial temperature distribution and transient thermal responses in the case of radiative heating with power of 50 W ($q_{app}'' = 1.3 \times 10^6$ W/cm^2). The thermal energy dissipates from the center of the irradiation (*i.e.*, the local hot spot) along the incident direction of the laser (Fig. 5(a)) and radially (Fig. 5(b)) by conduction through the powder bed. Under locally concentrated heating with moderate secondary heat dissipation through convection and radiation on the exterior surfaces, conduction is the principal process governing both the local and the overall heat transfer characteristics. Convection effects in the chamber should be minimized to prevent the material losses that can arise due to blowing and oxidation of the material. As this process is dominated by conduction, heat dissipation or transfer in a solid media is explained by the Fourier's law of conduction (Eq. (2)). Based on the relationship, we investigate local and overall heat transfer characteristics analytically. In a powder bed system (shown in Fig. 3), these characteristics can be determined by the effective properties of the powder bed, the input heating power, and the exposure time [8,20,25]. The absorbed energy can be quantified in terms of these parameters. Herein, we consider macroscopic approaches based on the plausible assumption that powder beds are homogeneous in confined domains [24,38]. When the target powder bed has high thermal conductivity, this will dominate the thermal response of the powder. Conduction effects within the powder bed lead to the incident thermal energy propagating towards the surrounding powder bed. The effective thermal conductivity of the Cu powder bed with high thermal conductivity plays a significant role in determining the local and overall heat transfer responses. From the contours and graphs in Fig. 5, we can see that the conductive heat spreading affects the overall temperature increase near the local hot spot and causes a significant temperature

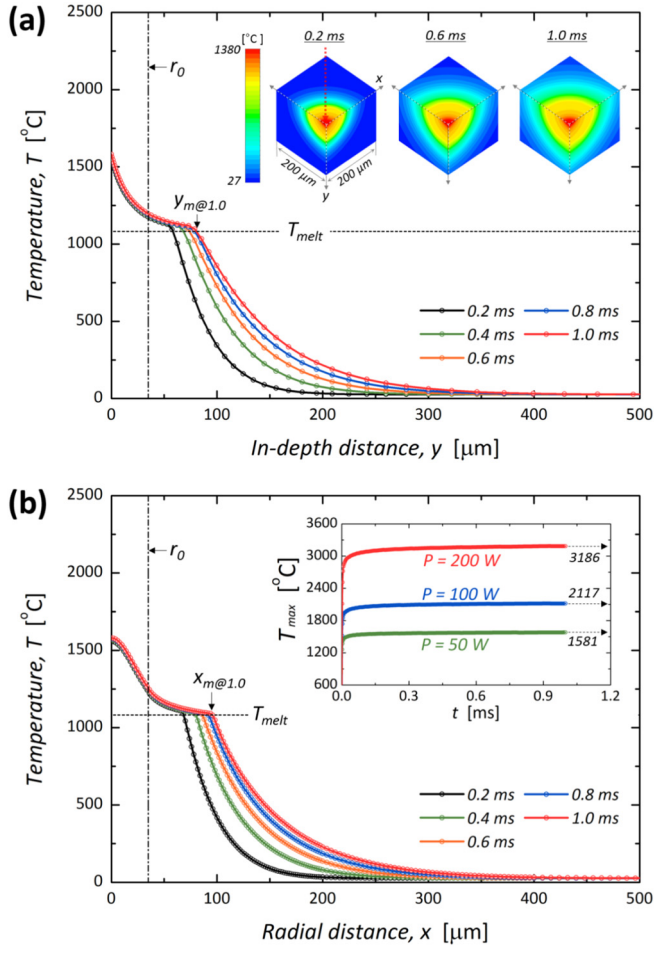

Fig. 5. Temperature distributions at $P = 50$ W with irradiation time along (a) the in-depth and (b) the radial direction (where T_{melt}, $y_{m@1.0}$ and $x_{m@1.0}$ indicate the melting point of the target material, the width of the melting pool along in-depth, and the radial direction, respectively). The insets in (a) and (b) show the contours of the temperature distribution near the heating spot and the transient maximum temperature with the input power, respectively.

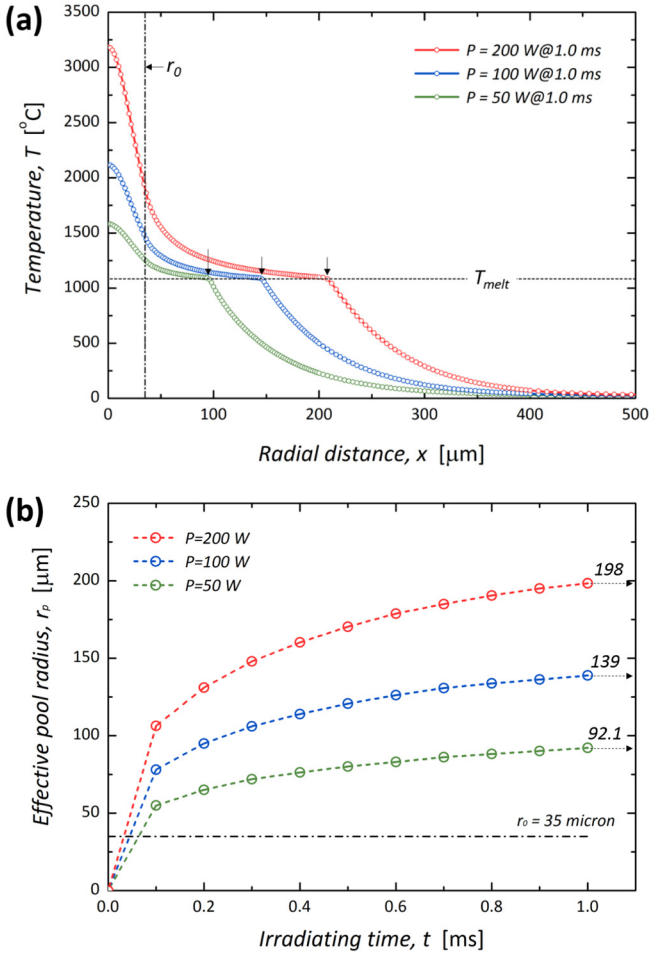

Fig. 6. Thermal responses according to the variation of input power. (a) Radial temperature distribution with various input powers at $t = 1.0$ ms (b) Effective pool radius, r_p according to exposure time and power.

gradient [20].

The spatial temperature distributions and maximum temperature depend on the exposure time and incident power. The local temperature is maximized with T_{max} at the center of the incident laser and decreases outwardly due to conduction. During local heating, the overall temperature increases with the exposure time. As the distance from the center increases to more than 400 μm in the lateral and vertical directions, there are no significant transient variations and there is not significant difference between the initial state, at room temperature, and the state after heating. The outward spatial gradient of the temperature diminishes with time and the increase in temperature reaches a plateau after as little as 1 ms exposure (inset of Fig. 5(b)) for each power condition. The temperature at the hot spot saturates at 1581 °C at 50 W and the transient outward increment decreases with time, resulting in less spatial deviation. This indicates that increasing the exposure time does not lead to an unlimited temperature increase; instead, it affects the transient thermal responses [25]. The transient characteristics below the critical temperature are confined by the energy balance between the external thermal load and the internal energy (*i.e.*, local temperature) increases within the thermal mass. By considering the energy balance, we can conclude that the incident power is a principal factor in determining the characteristic maximum temperature at the heating point, T_{max} [25]. This explains the results that, although the cases with different incident powers all saturate after an exposure time of 1 ms, they have different saturation temperatures: 1581, 2117, and 3186 °C with 50, 100, and 200 W, respectively (inset of Fig. 5(b)).

3.1.2. Prediction of the size of the molten pool

Spatial and transient characteristics impose restrictions on the size of the molten pool. This is the area that has transitioned from a solid state to a liquid-phase state. It varies with the exposure time and heating power. Fig. 6(a) shows that the spatial temperature gradient and consequential melting area should be strongly dependent on the input power. The molten area forms where the local temperature is higher than T_{melt}, the melting point of the target material. In the case of 50 W incident power at the saturation condition after 1 ms exposure, the characteristic lengths along the *x*- and *y*-axes are 95.4 and 80.4 μm, respectively (as indicated in Fig. 5). When higher incident power is used for local heating, larger areas melt. Incident powers of 100 and 200 W result in characteristic radii of 145.5 and 207.5 μm, respectively (Fig. 6(a)). The effective size of the pool is determined by the local temperature predictions as follows:

$$x_m \equiv Max(x)\,|_{T > T_{melt}},\ y_m \equiv Max(y)\,|_{T > T_{melt}} \tag{5}$$

$$r_{eff} = 2\pi x_m \bullet y_m / 2\pi \sqrt{(x_m^2 + y_m^2)/2} \tag{6}$$

where x_m, y_m, T_{melt}, and r_{eff} are, respectively, the distance from the center along the *x*- and *y*-axes, melting point of the target material, and effective radius of the elliptical melted pool. Fig. 6(b) shows that the effective melting area is governed by variations in the input power. All cases lead to expansion of the melting area over beyond the radius of

the incident laser source, r_0, which was 35 μm. This is why conductive heat dissipation through a powder bed can be used to control the accuracy of the target pattern. Even after 0.2 ms exposure with the lowest power of 50 W, the affected area (~62.6 μm) is larger than the area of the laser. The molten area expands with time, but the rate of expansion diminishes significantly when t is up to 1.0 ms because the energy balance reaches equilibrium. There are fewer transient temperature variations near 1.0 ms exposure as the internal energy absorption converges to equilibrium. This leads to consequential saturation of the expansion of the melting area.

Having characterized the local and the overall heat transfer, it should be possible for us to specify design guidelines for controlling the melting or sintering of the target material. First, the characteristic length of the molten pool depends strongly on the intrinsic thermal conduction properties of the pool material. These give rise to variations in the over-expanded melting area ($r_{eff} > r_0$) with the laser radius and power. It cautions us that precise line width control is required. To achieve a particular desired result of prescribed workpiece structures, all parameters must be optimized. High-input power lasers, *i.e.*, high surface heat flux concentrated on a target area, are required to obtain sufficient thermal energy for practical applications such as multi-compound sintering or full melting. However, unconstrained increases in input power result in widening of the melting pool – preventing precise pattern control and resultant inaccurate or coarse patterning on the target structure. Excessive exposure time (over 1.0 ms), which is equivalent to a varying velocity, after reach an equilibrium state does not have significant impacts on local sintering or melting. By considering the transient characteristics, a feasible parameter set based on either the velocity or the exposure time of the laser can be specified. This can be used to scan planar targets with SLM technology. Uncontrolled or oversized melting pools cause the precision of the pattern shape and line width to deteriorate. This is because the over-exposed energy is accumulated and propagates conductively through the bulk powder bed until the corresponding equilibrium state is reached.

3.2. Required transient thermal response for glass-metal synthesis: cooling rate

Fig. 7 shows the transient thermal response of the temperature decrease during cooling. This occurs when the radiative heat source is switched off, after which the system cools quickly. When we turn off the radiative heat source of the laser after 1 ms of heating, the local temperature at the point directly heated by the laser decreases significantly. Although the heating power affects the saturation temperature, local temperatures decrease rapidly towards the temperature of the exterior; room temperature is reached in approximately 0.4 ms. Conduction effects accompanied by fast and concentrated temperature variations were found to dominate both local transient heating and cooling. The local temperature rapidly approaches the exterior temperature as the heating preceding the cooling was confined to a local rather than heating the entire target thermal mass, as in a typical casting process. We define the apparent cooling rate as $(T_{max} - T_{melt})/\triangle t$, where T_{max} and $\triangle t$ are the maximum temperature and time from the start of the cooling to the moment when the local temperature reaches T_m, respectively. The evaluated cooling rates are extremely high, over 10^6 K/s and they vary almost linearly with the heating power. The high cooling rates evaluated must be one of greatest advantages of using SLM for material synthesis [47]. The high cooling rate following the material melting suppresses the growth of crystalline structures and enables us to fabricate amorphous structures for synthesis of 'metallic glasses.' [11,47,48] To obtain glass compositions, the local cooling rate should be sufficiently high to bypass the 'crystalline nose' in the continuous cooling transformation diagram, as shown schematically in Fig. 7 [9]. In actual SLM and other manufacturing methods, the dynamic behavior of the heating affects the bulk temperature increase of the target thermal mass. However, we can evaluate the exposure time required in terms of static local heating without taking into account any dynamic behaviors. Using a unit-cell specification for the heating and cooling of a local spots without any auxiliary bulk temperature heating, the desired exposure time and following cooling duration can be calculated. To obtain an amorphous solid, the actual cooling rate must be higher than the threshold for avoiding the 'crystalline nose' on the continuous cooling transformation diagram [11]. The glass transformation should be regarded as a kinetic process that occurs during local melting within a critical time period [9,49]. The very short cooling times required to induce metallurgical processes such as vitrification should be mentioned in guidelines for using lasers for pattern drawing. The time for cooling can be used to deduce velocity of the laser, which controls consequential equivalent cooling period after the heating [50].

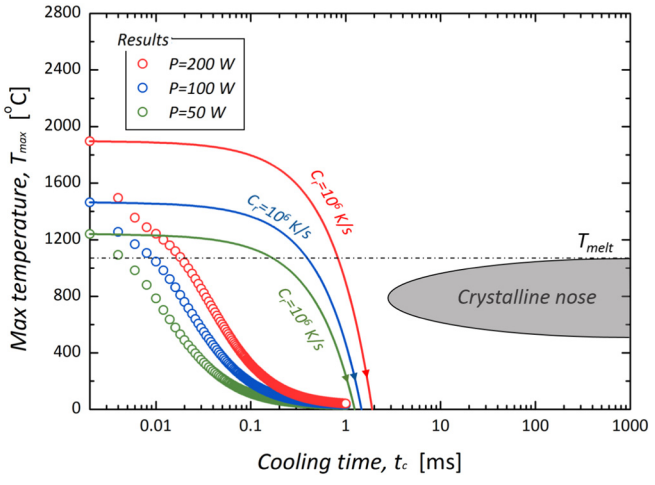

Fig. 7. Transient variation of the local temperature at the heated spot (T_{max}) with a schematic continuous cooling diagram. At higher cooling rates, which do not cross the crystalline nose, glassy metal formation occurs through direct vitrification. Hollow dots and solid lines indicate results from the transient cooling after the showdown of the laser power and analytic predictions of temperature decrease with the cooling rate (c_r) of 10^6 K/s, respectively.

3.3. Homogeneous and confined heat treatment: thermal Marangoni effect

Using SLM should lead to homogeneous solidifications and accurate patterns. The parameters must be carefully controlled to ensure the best results. By using locally concentrated heat radiation from a laser, the target material is heated to beyond the melting temperature in milliseconds. High temperature gradients as well as transient variations arising in the local molten pool generate thermocapillary forces [18,51]. The aforementioned local heat transfer characteristics imply that SLM, which uses a remarkably concentrated thermal load on a local spot, should be accompanied by secondary convection in the molten pool: thermal Marangoni flow [51–53]. When this thermocapillary force is present, vortices are generated in the liquid, and the heat and mass transfer characteristics can be affected. This means that the molten zone has clear dependence on solidification during the thermal process of SLM [18,54]. This convective flow has been pointed out as a detrimental factor to the production of uniform and homogeneous structures in a locally molten area [51]. The Marangoni flow is induced by surface tension gradients. These are caused by temperature gradients. The flow is quantified numerically using the Marangoni number, Ma [51,55]:

$$Ma = -\frac{d\sigma}{dT}\frac{\Delta TL}{\mu\alpha_t} \propto \beta,\ \beta = \Delta TL \tag{7}$$

where σ, L, μ, and α_t are the surface tension, characteristic length, dynamic viscosity, and thermal diffusivity, respectively. Each variable is a

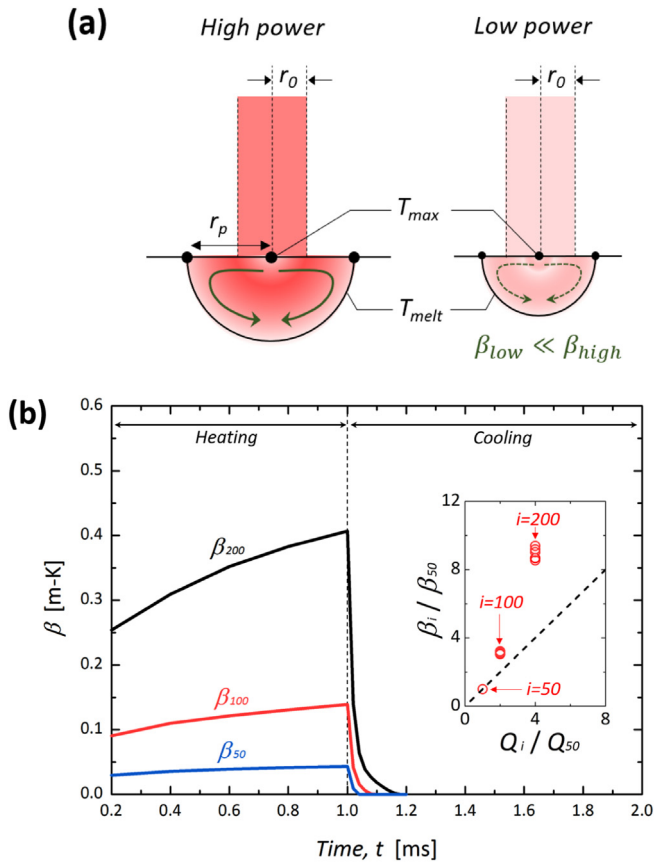

Fig. 8. Effects of the incident power on characteristics of the molten area and the induced Marangoni force. (a) Schematic diagram of vortex pair generation in a liquid molten pool with a negative surface tension gradient, and the resulting widening of the pool. (b) Quantitative variation of the transient Marangoni factor β according to incident power. The inset presents the impact of the incident power Q on the resultant Marangoni factor. Herein, the subscript of β and Q indicates the incident laser power.

property of the target material, apart from the local temperature difference ΔT and L, which depend on the input parameters. When a local spot is subjected to intense radiation, the temperature-induced surface tension gradient plays a more significant role than the concentration gradients [18]. The characteristic length is a substitute for the effective radius of r_{eff}. The negative surface tension gradient is 1257–0.2(T-1356) mN/m in the case of a Cu powder bed [56]. We can predict that there will be a vortex pair with radially outward flow. The flow will be from a weakly attractive area with low σ and a high temperature to a strongly attractive region with high σ, as schematically illustrated in Fig. 8(a). The effects of these vortices are quantified as a function of input power and exposure time in Fig. 8(b). As mentioned regarding transient local temperature variations and their impact on the effective pool radius, the Marangoni factor β increases with exposure time. Using a higher power leads to a higher β value and a steeper gradient with respect to time.

If we wish to consider it macroscopically, the propagation of the absorbed thermal energy can be treated as a simplified thermal conduction circuit through a solid or quasi-solid medium. When we assume that the confined medium has isotropic thermal properties, and that there are no significant energy losses, the effective heat flow dissipates through the medium following its absorption from the incident laser. This is formulated by Fourier's law of heat conduction as follows [43]:

$$Q''_{eff} = -k\nabla TA \propto -k\beta \tag{8}$$

where A is the unit area of the target unit cell. This relationship tells us that β is an indirect indicator of the heat flow; the effective heat flow through the target medium is proportional to β. Herein, the subscript of β in Fig. 8 indicates the incident laser power. From the results shown in the inset of Fig. 8(b), however, we can see that β is valued over linear proportion to the input power. When the input power increases from 50 to 100 and 200 W, β_i/β_{50} increases by over 304.3% and 853.7%, respectively. The subscript indicates the corresponding input power. Higher incident powers lead to stronger Marangoni force due to the large temperature difference (ΔT) and enlarged characteristic lengths (r_{eff}). The effects of the Marangoni phenomenon become more pronounced as the power increases as $\beta_i/\beta_{50} \approx B{\cdot}Q_i/Q_{50}$, where B is a coefficient over unity. In the case of a radially outward vortex pair (Fig. 8(a)), they bring about a lateral widening of the molten area due to convective heat dissipation. This degrades the accuracy of the pattern width control. Uncontrollable pattern sizes (melting area size) caused by secondary vortex flows can arise due to Marangoni effect's significant influence on the quasi-effective heat flow [17,43]. In the case of Cu, this secondary thermal effect caused by the Marangoni force can become exaggerated due to the high thermal conductivity of Cu. This results in non-spherical melting and anisotropic patterns [50]. Therefore, we have to remind that the dependency of β on the input power should be analyzed carefully to enable us to achieve precise and accurate control of the shape and width (or depth) of the molten pool. We can obtain an upper limit by noting that the local temperature should not be much higher than the boiling point (*i.e.*, $T_{max} < T_{boiling}$, where $T_{boiling}$ of Cu is 2562 °C) to minimize material losses due to evaporation and the consequent uneven surface profile.

4. Conclusion

SLM is a promising technique for manufacturing complicated components and synthesizing glassy metals. These undergo amorphous vitrification during thermal treatment. To create novel materials and workpieces, we must understand the local heat transfer characteristics during SLM. This will enable us to obtain reliably target objects that have the desired pattern shapes, dimensions, and mechanical performances. We presented a methodology to evaluate the local/overall heat transfer characteristics of materials undergoing the SLM process and determined the most prominent transient effects of the principal parameters. Through exemplary approaches and analytical demonstrations, we showed how to control the local melting and sequent solidification of the powdered target material. The radiated power and exposure time were found to be of importance to determine the local heat transfer characteristics. We also discussed the role of secondary local advection in the molten pool, the causes of thermally induced Marangoni flow, and approaches to reducing the detrimental effects of this flow. The input power should be limited as it has a significant effect on both the spatial and the transient heat transfer characteristics. The characteristics of radiative heating accompanied by secondary heat dissipation over a metallurgic powder bed should be optimized by selecting appropriate values for the exposure time and the input power. Our demonstration can be used to test SLM systematically and tailor it to novel alloy compositions. In the future, dynamic multi-scanning simulations will be performed and different scanning strategies will be evaluated numerically and compared to experimental SLM. This will optimize the parameters to obtain the greatest improvement in SLM performance along the basis of the proposed numerical analysis. We are going to improve our numeric approaches by incorporating a variety of techniques from material science and the theory of heat transfer into our simulations. This will lead to making a platform in SLM process guaranteeing its feasibility and wider applicability.

Acknowledgments

B.S. Kim acknowledges the NRF Korea for support through the Alexander von Humboldt Foundation for support through a Humboldt Research Fellowship (3.5-KOR/1159778 STP). Also, this work was

supported by the Human Resources Development Program (No. 20174030201720) and the Korea Government (MOTIE) (No. 20193310100030) of the Korea Institute of Energy Technology Evaluation and Planning (KETEP), grant funded by the Korea government Ministry of Trade, Industry and Energy, and supported (in part) by the Yonsei University Research Fund (Yonsei Frontier Lab. Young Researcher Supporting Program) of 2018.

References

[1] A. Bruce-Lockhart, 10 ways 3D printing can change the world, World Economic Forum (2015) https://www.weforum.org/agenda/2015/06/3d-printing-save-the-world/.
[2] M. Agarwala, D. Bourell, J. Beaman, H. Marcus, J. Barlow, Direct selective laser sintering of metals, Rapid Prototyping J 1 (1995) 26–36.
[3] E.C. Santos, M. Shiomi, K. Osakada, T. Laoui, Rapid manufacturing of metal components by laser forming, Int. J. Mach. Tools Manuf. 46 (2006) 1459–1468.
[4] C. Ladd, J.H. So, J. Muth, M.D. Dickey, 3D printing of free standing liquid metal microstructures, Adv. Mater. 25 (2013) 5081–5085.
[5] W.E. Frazier, Metal additive manufacturing: a review, J. Mater. Eng. Perform. 23 (2014) 1917–1928.
[6] D.D. Gu, W. Meiners, K. Wissenbach, R. Poprawe, Laser additive manufacturing of metallic components: materials, processes and mechanisms, Int. Mater. Rev. 57 (2012) 133–164.
[7] J.P. Kruth, G. Levy, F. Klocke, T.H.C. Childs, Consolidation phenomena in laser and powder-bed based layered manufacturing, CIRP Ann-Manuf. Technol. 56 (2007) 730–759.
[8] B. Song, S. Dong, H. Liao, C. Coddet, Process parameter selection for selective laser melting of Ti6Al4V based on temperature distribution simulation and experimental sintering, Int. J. Adv. Manuf. Technol. 61 (2012) 967–974.
[9] S. Pauly, L. Löber, R. Petters, M. Stoica, S. Scudino, U. Kühn, J. Eckert, Processing metallic glasses by selective laser melting, Mater. Today 16 (2013) 37–41.
[10] A.L. Greer, Metallic Glasses, Science 267 (1995) 1947–1953.
[11] A. Inoue, A. Takeuchi, Recent development and application products of bulk glassy alloys, Acta Mater. 59 (2011) 2243–2267.
[12] E.S. Park, M. Ohnuma, D.H. Kim, Anomalous glass transition behavior in Cu–Zr–Sn alloy system, J. Alloy Compd. 509S (2011) S52–S55.
[13] L. Rickenbacher, T. Etter, S. Hovel, K. Wegener, High temperature material properties of IN738LC processed by selective laser melting (SLM) technology, Rapid Prototyping J 19 (2013) 282–290.
[14] G. Kasperovich, J. Hausmann, Improvement of fatigue resistance and ductility of TiAl6V4 processed by selective laser melting, J. Mater. Process. Technol. 220 (2015) 202–214.
[15] R. Engeli, T. Etter, S. Hovel, K. Wegener, Processability of different IN738LC powder batches by selective laser melting, J. Mater. Process. Technol. 229 (2016) 484–491.
[16] L. Kashdan, C.C. Seepersad, M. Haberman, P.S. Wilson, Design, fabrication, and evaluation of negative stiffness elements using SLS, Rapid Prototyping J 18 (2012) 194–200.
[17] L.X. Yang, X.F. Peng, B.X. Wang, Numerical modeling and experimental investigation on the characteristics of molten pool during laser processing, Int. J. Heat Mass Transf. 44 (2001) 4465–4473.
[18] O.B. Kovalev, A.M. Gurin, Multivortex convection of metal in molten pool with dispersed impurity induced by laser radiation, Int. J. Heat Mass Transf. 68 (2014) 269–277.
[19] H. Schleifenbaum, W. Meiners, K. Wissenbach, C. Hinke, Individualized production by means of high power selective laser melting, CIRP Ann-Manuf. Technol. 2 (2010) 161–169.
[20] L.-E. Loh, C.-K. Chua, W.-Y. Yeong, J. Song, M. Mapar, S.-L. Sing, Z.-H. Liu, D.-Q. Zhang, Numerical investigation and an effective modelling on the selective laser melting (SLM) process with aluminium alloy 6061, Int. J. Heat Mass Transf. 80 (2015) 288–300.
[21] I. Yadroitsev, P. Bertrand, I. Smurov, Parametric analysis of the selective laser melting process, Appl. Surf. Sci. 253 (2007) 8064–8069.
[22] J.P. Kruth, X. Wang, T. Laoui, L. Froyen, Lasers and materials in selective laser sintering, Assem. Autom. 23 (2003) 357–371.
[23] J.F. Li, L. Li, F.H. Stott, Comparison of volumetric and surface heating sources in the modeling of laser melting of ceramic materials, Int. J. Heat Mass Transf. 47 (2004) 1159–1174.
[24] K. Zeng, D. Pal, B. Stucker, A review of thermal analysis methods in laser sintering and selective laser melting, 23rd Annual International Solid Freeform Fabrication Symposium - an Additive Manufacturing Conference, SFF 2012, 2012, pp. 796–814.
[25] M. Shiomi, A. Yoshidome, F. Abe, K. Osakada, Finite element analysis of melting and solidifying processes in laser rapid prototyping of metallic powders, Int. J. Mach. Tools Manuf. 39 (1999) 237–252.
[26] B.S. Kim, B.S. Kwak, S. Shin, S. Lee, K.M. Kim, H.I. Jung, H.H. Cho, Optimization of microscale vortex generators in a microchannel using advanced response surface method, Int. J. Heat Mass Transf. 54 (2011) 118–125.
[27] A. Inoue, W. Zhang, T. Zhang, K. Kurosaka, High-strength Cu-based bulk glassy alloys in Cu–Zr–Ti and Cu–Hf–Ti ternary systems, Acta Mater. 49 (2001) 2645–2652.
[28] D.D. Gu, Y.F. Shen, Development and characterisation of direct laser sintering multicomponent Cu based metal powder, Powder Metall. 49 (2006) 258–264.
[29] R. Li, Y. Shi, J. Liu, Z. Xie, Z. Wang, Selective laser melting W–10 wt.% Cu composite powders, Int. J. Adv. Manuf. Technol. 48 (2010) 597–605.
[30] D. Dai, D. Gu, Thermal behavior and densification mechanism during selective laser melting of copper matrix composites: simulation and experiments, Mater. Des. 55 (2014) 482–491.
[31] P.K. Deshpande, J.H. Li, R.Y. Lin, Infrared processed Cu composites reinforced with WC particles, Mater. Sci. Eng. A 429 (2006) 58–65.
[32] P.A. Lykov, et al., Selective laser melting of copper, Mater. Sci. Foru 843 (2016) 284.
[33] S.D. Jadhav, et al., Influence of selective laser melting process parameters on texture evolution, J. Mater. Process. Tech. 270 (2019) 47.
[34] J.H. Lienhard, A Heat Transfer Textbook, Courier Corporation, 2011.
[35] A.V. Gusarov, I. Yadroitsev, P. Bertrand, I. Smurov, Heat transfer modelling and stability analysis of selective laser melting, Appl. Surf. Sci. 254 (2007) 975–979.
[36] A.V. Gusarov, J.P. Kruth, Modelling of radiation transfer in metallic powders at laser treatment, Int. J. Heat Mass Transf. 48 (2005) 3423–3434.
[37] F. Thümmler, R. Oberacker, I.o. Materials, An Introduction to Powder Metallurgy, Institute of Materials, 1993.
[38] I.A. Roberts, C.J. Wang, R. Esterlein, M. Stanford, D.J. Mynors, A three-dimensional finite element analysis of the temperature field during laser melting of metal powders in additive layer manufacturing, Int. J. Mach. Tools Manuf. 49 (2009) 916–923.
[39] M. Rombouts, L. Froyen, A.V. Gusarov, E.H. Bentefour, C. Glorieux, Photopyroelectric measurement of thermal conductivity of metallic powders, J. Appl. Phys. 97 (2005) 024905.
[40] R.M. German, Powder Metallurgy Science, 2nd ed., Metal Powder Industries Federation, Princeton, N.J, 1994.
[41] Y.A. Çengel, M.A. Boles, Thermodynamics: An Engineering Approach, 6th ed., McGraw-Hill, Boston, 2008.
[42] ANSYS Fluent V.15.0 Theory Guide, ANSYS, 2013.
[43] F.P. Incropera, Fundamentals of Heat and Mass Transfer, 6th ed., John Wiley, Hoboken, N.J, 2007.
[44] Y.A. Çengel, A.J. Ghajar, Heat and Mass Transfer: Fundamentals & Applications, McGraw-Hill, New York, 2011.
[45] W.-L. Chen, Y.-C. Yang, H.-L. Lee, Estimating the absorptivity in laser processing by inverse methodology, Appl. Math. Comput. 190 (2007) 712–721.
[46] I. Yadroitsev, I. Smurov, Selective laser melting technology: from the single laser melted track stability to 3D parts of complex shape, Phys. Procedia 5 (2010) 551–560.
[47] W.-C. Huang, C.-S. Chuang, C.-C. Lin, C.-H. Wu, D.-Y. Lin, S.-H. Liu, W.-P. Tseng, J.-B. Horng, Microstructure-controllable laser additive manufacturing process for metal products, Phys. Procedia 56 (2014) 58–63.
[48] W.H. Wang, C. Dong, C.H. Shek, Bulk metallic glasses, Mater. Sci. Eng. R-Rep. 44 (2004) 45–89.
[49] J.J. Han, C.P. Wang, X.J. Liu, Y. Wang, Z.K. Liu, T.Y. Zhang, J.Z. Jiang, Abnormal correlation between phase transformation and cooling rate for pure metals, Sci. Rep. 6 (2016) 22391.
[50] I. Yadroitsev, A. Gusarov, I. Yadroitsava, I. Smurov, Single track formation in selective laser melting of metal powders, J. Mater. Process. Technol. 210 (2010) 1624–1631.
[51] M. Rombouts, J.P. Kruth, L. Froyen, P. Mercelis, Fundamentals of selective laser melting of alloyed steel powders, CIRP Ann-Manuf. Technol. 55 (2006) 187–192.
[52] F.K. Chung, P.S. Wei, Mass, momentum, and energy transport in a molten pool when welding dissimilar metals, J. Heat Transf. 121 (1999) 451–461.
[53] S.J. Vanhook, M.F. Schatz, J.B. Swift, W.D. McCormick, H.L. Swinney, Long-wavelength surface-tension-driven Benard convection: experiment and theory, J. Fluid Mech. 345 (1997) 45–78.
[54] Y. Pengpeng, G. Dongdong, Molten pool behaviour and its physical mechanism during selective laser melting of TiC/AlSi10Mg nanocomposites: simulation and experiments, J. Phys. D-Appl. Phys. 48 (2015) 035303.
[55] M.F. Schatz, S.J. Vanhook, W.D. McCormick, J.B. Swift, H.L. Swinney, Onset of surface-tension-driven benard convection, Phys. Rev. Lett. 75 (1995) 1938–1941.
[56] M. Taihei, F. Hidetoshi, U. Takaharu, K. Masayoshi, N. Kiyoshi, Measurement of surface tension of molten copper using the free-fall oscillating drop method, Meas. Sci. Technol. 16 (2005) 432.